Journal of Materials Research and Technology 28 (2024) 1359–1369

Contents lists available at ScienceDirect

Journal of Materials Research and Technology

journal homepage: www.elsevier.com/locate/jmrt

Mechanical and piezoresistive properties of GNP/UHMWPE composites and their cellular structures manufactured via selective laser sintering

Muhammad Umar Azam [a], Andreas Schiffer [a,*], S. Kumar [b,**]

[a] Department of Mechanical and Nuclear Engineering, Khalifa University, P.O. Box 127788, Abu Dhabi, United Arab Emirates
[b] James Watt School of Engineering, University of Glasgow, Glasgow, G12 8QQ, UK

ARTICLE INFO

Handling Editor: L Murr

Keywords:
Additive manufacturing
Self-sensing
Graphene
Lattice structure
3D printing

ABSTRACT

In this study, we describe the development of composites comprising ultra-high molecular weight polyethylene (UHMWPE) reinforced with graphene nanoplatelets (GNP), specifically designed for additive manufacturing (AM) of self-sensing structures through selective laser sintering (SLS). We employed ball-milled GNP/UHMWPE powder feedstocks to fabricate standard test specimens and 2D cellular structures with varying GNP content. A comprehensive assessment of their mechanical and piezoresistive properties was carried out under uniaxial tensile loading. The incorporation of 1.5 wt% GNPs into UHMWPE demonstrated a notable increase in crystallinity by ~28 % and a significant reduction in porosity by about 98 %. These enhancements contributed to a substantial improvement in both strength (~21 %) and elastic modulus (~40 %). Moreover, the introduction of 1.5 wt% GNPs resulted in the formation of electrically percolated composites characterized by prominent piezoresistive behavior. These composites exhibited gauge factors ranging from 9.6 to 18 under uniaxial tensile loading. During cyclic tensile loading, the GNP/UHMWPE composite displayed hysteresis in its piezoresistive response due to viscoelasticity, impeding an immediate return to its original state. Additionally, the gauge factors of the 2D cellular structures generally demonstrated lower values compared to those of the parent composite, scaling proportionally with the effective elastic modulus.

1. Introduction

Ultra-high molecular weight polyethylene (UHMWPE) is a semi-crystalline thermoplastic polymer with exceptional properties including high impact and wear resistance, good lubricity, chemical inertness against numerous acids and alkalis, biocompatibility and thermal stability [1,2]. Due to its superior physical and mechanical characteristics, UHMWPE has been utilized in a variety of fields, including orthopedics where it has been widely used to cover articular surfaces of artificial joints [1,3]. However, the high melt viscosity (up to 1×10^8 Pa s) and molecular weight ($\geq 1.5 \times 10^6$ g mol^{-1}) of UHMWPE [4] limit its ability to be shaped into complex structures, which is a considerable drawback for the manufacture of orthopedic implants [5]. Another potential risk factor associated with the use of UHMWPE-based orthopedic implants is osteolysis caused by wear debris [6], which might require implant replacement.

Additive manufacturing (AM), also known as 3D printing, has significantly relaxed the extant manufacturing constraints in the past decade. AM offers numerous advantages compared to conventional manufacturing methods, such as increased design flexibility, rapid prototyping capabilities, enhanced precision in component dimensions, and reduced material wastage throughout the production [7]. Among the array of AM techniques, selective laser sintering (SLS) stands out for several reasons. Notably, it eliminates the need for support structures, allows for the production of sizable batches, imparts relatively high strength to printed structures, and enables the recycling of unfused powder [8]. In the SLS process, powder particles are evenly distributed over the printing bed and selectively sintered layer by layer using a laser beam (typically a CO_2 laser) within an enclosed chamber. Upon completion, the sintered parts are extracted from the chamber, with the unsintered powder surrounding the printed parts removed. An advantage of SLS lies in its capability to sinter intricate parts without requiring a mold, distinguishing it from other sintering processes. Despite its numerous benefits, SLS does have practical limitations, particularly concerning the selection of feedstock polymers. This limitation arises from the reliance on intricate diffusion processes, necessitating specific

* Corresponding author.
** Corresponding author.
E-mail addresses: andreas.schiffer@ku.ac.ae (A. Schiffer), msv.kumar@glasgow.ac.uk (S. Kumar).

https://doi.org/10.1016/j.jmrt.2023.12.089
Received 18 November 2023; Received in revised form 9 December 2023; Accepted 9 December 2023
Available online 12 December 2023

combinations of thermophysical and thermomechanical characteristics [9].

Currently, only a few studies on the processing of UHMWPE via SLS have hitherto been reported in the literature. Early work on this subject was reported by Rimell et al. [10] utilized non-commercial SLS equipment to 3D print basic linear shapes from UHMWPE powder. However, they were unable to print more complex geometries due to the high shrinkage and porosity of the printed parts. In 2010, Goodridge et al. [11] succeeded in SLS 3D printing of UHMWPE tensile and flexural specimens using an optimized set of process parameters. However, their printed specimens exhibited poor mechanical characteristics due to the narrow sintering window of UHMWPE. Khalil et al. [12,13] investigated the impact of laser power on the flexural and tensile characteristics of SLS-processed UHMWPE specimens. They noticed an improvement in the mechanical properties of printed specimens at higher laser power, but the dimensional accuracy could not be maintained. To improve the mechanical characteristics of laser-sintered UHMWPE, Song et al. [3] applied post-heat treatment on SLS-processed tibial implants, which increased the components' tensile strength (~71 %). The principal obstacles in UHMWPE processing via SLS involve the formation of a dense powder bed (hard caking) and the potential for the sintered part to curl or slide during the printing process, as highlighted in our recent study [14], leading to potential print failures. Recently, Zhu et al. [15] added fumed silica as an anti-caking agent to facilitate the SLS processing of UHMWPE. While the caking tendency of the powder was significantly reduced, it degraded the mechanical characteristics of the printed specimens.

The potential of SLS 3D-printed UHMWPE components for utilization in practical applications has remained largely untapped due to the inherent challenges posed by the narrow sintering window of UHMWPE. These challenges encompass issues such as warping and the compaction or hard caking of the powder bed [14,15]. In addition, it is difficult to manufacture defect-free UHMWPE components using SLS, and these imperfections might increase to a critical size in service under repetitive mechanical loading [16]. As a result, monitoring structural deformation and damage in real-time is crucial for spotting structural integrity issues early on, allowing for corrective action to be taken. One way to achieve this is to integrate the sensing functionality in the structure itself through the development of self-sensing composites. In recent years, AM has emerged as a viable technology for developing electrically conductive polymer-based composites with self-sensing capabilities [7,17,18], in addition to improving the mechanical properties of the materials [19]. Graphene has recently attracted a lot of attention as a conductive filler because of its exceptional electrical, mechanical, thermal and chemical properties [20]. Due to its high elastic modulus (0.5–1 TPa), exceptional in-plane strength and surface area, it is of great interest as reinforcement in structural composites [21]. Multi-layer sheets of graphene stacked upon each other are known as graphene nanoplatelets (GNP). GNPs are easier to disperse in the polymers than CNTs, resulting in a more uniform dispersion of the reinforcing phase in the matrix [20]. Moreover, it has been shown that graphene is effective in enhancing the lubrication properties in load-bearing components [20], resulting in less wear and debris which is a desirable characteristic for orthopedic implants. Furthermore, GNPs are considered as biocompatible due to their inert behavior provided by the planar carbon structure and have promising applications in biomedical and biotechnology fields [22]. However, a few reports have shown that graphene's cytotoxicity is dose-dependent [23].

While a few recent studies explored the development of polymer-based composites through SLS [24,25], there exists a notable dearth of literature on SLS 3D printed GNP/UHMWPE composites. The principal objective of this study is to additively manufacture self-sensing GNP/UHMWPE composites and their 2D cellular structures utilizing the SLS technique. A low-energy ball-milling process is harnessed to synthesise GNP/UHMWPE composite powders with varying GNP concentrations, subsequently serving as the raw material for SLS 3D printing of electrically conductive bulk and two-dimensional lattice structures. Comprehensive experimental assessments are undertaken to evaluate the mechanical performance, as well as the piezoresistive strain- and damage-sensing capabilities of the 3D-printed specimens under both quasi-static and cyclic loading conditions. Furthermore, this study engages in an in-depth exploration of the intricate interplay between processing, structure, and property relationships.

2. Experimental details

2.1. Materials

Ultra-high molecular weight polyethylene (UHMWPE) with a molecular weight of $>4.5 \times 10^6$ g mol^{-1} was purchased from Nanoshel® (India) and has a purity level of 99.99 % with an average particle size of 130 ± 33 μm. Graphene powder (P-ML20®), also referred to as graphene nanoplatelets (GNP) in this study, was purchased from Enerage Inc (Taiwan). P-ML20® is composed of multi-layer sheets (5–8) of graphene stacked upon each other. The average thickness of the sheets is ~5 nm and the electrical conductivity is ≥ 1600 S cm^{-1} (according to the supplier). Additional information on the structural and morphological characterization of the as-received GNPs can be found in **Section S2** (Supplementary Information).

2.2. Feedstock preparation for SLS

The UHMWPE powder was mixed with different weight fractions of GNPs using a planetary ball mill (Pulverisette 5, Fritsch, Germany) operated at 200 rpm for 45 min with a 10:1 ball-to-powder ratio. In the following, the composite powders with 1, 1.5 and 2 wt% GNP loading are designated as U-1, U-1.5, and U-2, respectively, while the neat as-received UHMWPE powder is denoted as U-0. As suggested in the literature [8,14], the powders were artificially aged to achieve consistency in the quality of all prints.

2.3. 3D printing

A Sharebot SnowWhite SLS 3D printer (Italy) was used to print standard test specimens and 2D lattice structures using the ball-milled GNP/UHMWPE powder feedstock. Note that the geometries and dimensions of the printed specimens are given in **Section 2.5**. Frequent challenges encountered during the sintering of UHMWPE, such as issues like warping and caking of the printed samples, were observed across various test prints, as detailed in **Section S1** (Supplementary Information). To address these issues effectively, we systematically modified the laser power, bed temperature (T_b), and laser scan rate, making incremental adjustments to identify an optimal combination of process parameters for each powder composition. A large number of test prints were executed to determine an optimal set of SLS process parameters that maximized the densification and strength of the 3D-printed GNP/UHMWPE samples. These optimal parameters are meticulously documented in Table 1. Powders with a larger GNP loading, for instance, were sintered at significantly lower bed temperatures to prevent caking issues due to the fact that carbonaceous nanofillers (e.g. CNTs, GNP) increase the thermal conductivity of the feedstock [14,26]. Also,

Table 1
SLS process parameters used in this study.

Parameter	U-0	U-1	U-1.5	U-2
Scan speed (points/sec)	12,000	12,000	12,000	12,000
Bed temperature (°C)	*145*	*143*	*142*	*142*
Layer height (mm)	0.1	0.1	0.1	0.1
Laser power (W)	8.4	8.4	8.4	8.4
Pre-heating time (sec)	3600	3600	3600	3600
Warming layer	20	20	20	20

GNP-coated feedstocks can absorb more laser energy which promote their melting compared to virgin feedstocks [14,26]. This implies that the addition of GNPs to the polymer powder requires overall shorter laser exposure (or less T_b). Additionally, the powder feedstock was pre-heated for 1 h to eliminate warpage, as recommended in the literature [5].

2.4. Characterization techniques

The morphologies of the powder feedstocks and fracture surfaces of the printed samples were analyzed using a high-resolution scanning electron microscope (FEI Nova NanoSEM 650). To prevent the charging effect, a sputter coater (JEC-3000FC, JEOL) was used to deposit a gold coating of thickness 10 nm on all samples before SEM imaging.

X-ray micro-computed tomography (μCT) images were acquired using a Phoenix nanotom® M nanoCT 3D scanner (GE Sensing & Inspection Technologies GmbH) to examine the microstructure of the 3D printed samples at a voxel resolution of 15 μm.

The thermal characteristics of the as-received UHMWPE and ball-milled GNP/UHMWPE powders were analyzed via differential scanning calorimetry (DSC 131 EVO, Setaram Instrumentation) performed in N_2 atmosphere at temperatures ranging from 25 to 200 °C using aluminium crucibles. The rate of heating and cooling was set to 10 °C min^{-1}. The degree of crystallinity, X, was determined by

$$X = \frac{\Delta H_m}{H_{100}}.100\% \quad (1)$$

where ΔH_m denotes the melting enthalpy of the sample under examination, and ΔH_{100} denotes the enthalpy of fusion of 100 % crystalline UHMWPE, $\Delta H_{100} = 289$ J g^{-1} [6].

Thermogravimetric analysis (TGA) (SDT-Q600, TA Instruments) was performed to investigate the thermal stability of all feedstock powders in N_2 atmosphere at temperatures ranging from 25 to 600 °C. The powder samples were placed in aluminium crucibles and were heated at a rate of 10 °C min^{-1}. Based on the obtained weight loss (%) vs. temperature curves, the thermal degradation temperatures, T_d, were obtained by determining the points of intersection between two tangents constructed at the starting onset and the completion onset, respectively.

2.5. Measurement of mechanical and piezoresistive properties

A Zwick-Roell (Z005) UTM with a 2.5 kN load cell was used to conduct *quasi-static monotonic tensile tests* on 3D printed dogbone-shaped specimens with a gauge section of 35 × 5 × 2 mm^3 (ASTM D638 Type IV standard). Furthermore, the same UTM was used to conduct uniaxial tensile tests on the printed 2D hexagonal and re-entrant lattice structures of 50 % relative density. The topology, size and architectural parameters of the lattice structures are shown in Fig. S10 and Table S1 (Supplementary Information). A crosshead speed of 2.5 mm min^{-1} was used for the latter tests.

In addition, two types of *cyclic tensile tests* were performed on the 3D-printed dogbone-shaped U-1.5 specimens at a constant loading/unloading rate of 2.5 mm min^{-1}. In *incremental cyclic loading*, the samples were subjected to five load-unload cycles with strain amplitudes of 0.25, 0.5, 1, 2, and 3 %, respectively. Once the desired strain level was reached in each load cycle, the samples were unloaded to zero stress without any holding period. In *strain-controlled cyclic loading*, samples were subjected to 100 load-unload cycles over a range of 1 % $\leq \varepsilon \leq$ 2 % without any holding period. Note that a maximum strain of 2 % was selected to prevent the sample from experiencing plastic deformation or failure, while a minimum strain of 1 % was set to ensure that the produced stresses remain tensile throughout the test. Due to the viscoelastic nature of UHMWPE, unloading to zero strain may induce compressive stresses in the test specimen.

During the mechanical tests explained above, the electrical resistance R of each sample was monitored *in situ* using a DMM 4050 Multimeter (Tektronix, USA), and the relative change in electrical resistance $\Delta R/R_0$ was determined, where R_0 denotes the initial zero load resistance, and $\Delta R = R - R_0$. As shown in Fig. S7 (Supplementary Information), the signals were acquired by clipping the probes of the multimeter onto a piece of copper foil placed between the specimen and the grips of the UTM. Note that PVC tape was used to shield the loading train from any potential charge leakage. The gauge factor, k, was used to quantify the piezoresistive sensitivity of the test specimens over a given strain interval $\Delta\varepsilon$.

$$k = \frac{\Delta(\Delta R/R_0)}{\Delta\varepsilon}. \quad (2)$$

It is important to note that at least three virgin samples were tested for each experiment described above to demonstrate that the obtained measurements are repeatable.

3. Results and discussion

3.1. Morphological and thermal characterization

SEM images of the as-received GNPs are presented in Fig. 1a, showing graphene sheets of size ~4 ± 1 μm. The SEM images of the UHMWPE powder (see Fig. 1b) show particles of irregular shape measuring ~130 ± 33 μm. At higher magnifications, the SEM images reveal that the UHMWPE particles consist of agglomerates of smaller particles held together by short fibrils. In Fig. 1c and Fig. S2 (Supplementary Information), SEM images of the GNP/UHMWPE composite powders are presented, showing smoother particle surfaces than the as-received UHMWPE powder after ball milling. Spherical particles with smooth surfaces are easier to spread on the print bed and form more uniform powder layers, which is a requirement for high-quality SLS prints [27]. Moreover, good dispersion of nanofillers was observed up to 1.5 wt% GNP loading in the UHMWPE matrix (see Figs. S2a–b, Supplementary Information); at higher GNP loadings (2 wt%) larger agglomerates of GNPs were observed on the UHMWPE particles, as seen from Fig. S2c.

The DSC curves for the GNP/UHMWPE powders obtained during the 2nd heating and cooling cycles are presented in Fig. 2a and b respectively. The heating curves (Fig. 2a) show that with increasing GNP loading, the melting peaks broadened, and the melting temperatures decreased slightly from 143 to 141 °C (see Table 2) owing to the high thermal conductivity of the GNPs. The cooling curves (Fig. 2b) show that the added GNPs slightly increased the powders' recrystallization temperatures (T_c), particularly for sample U-2, which further constrained the sintering window [14]. Note that the increase in T_c is explained by the fact that nanofillers act as heterogeneous nucleation sites, facilitating the crystallization of the polymer matrix [28,29]. Hence, the composites with higher GNP loading were printed at lower bed temperatures (T_b) to ensure that the non-laser-irradiated powder particles remained unfused following the SLS process. The degree of crystallinity (X) of GNP/UHMWPE composites was found to increase (from 38 to 49 %) with increasing GNP loading up to 1.5 wt%, after which it slightly decreased (46 %) due to the presence of agglomerated GNPs (see Table 2), which act as contaminants/defects and impede the polymer chains to align during crystallization [30].

The TGA results of the GNP/UHMWPE powders are presented in Fig. 2c and d and Table 2, showing that the addition of GNPs increased the thermal degradation temperatures (T_d) of the composites from 462 to 468 °C. Since the GNPs have higher thermal conductivity and stability, they impede the mobility of polymeric chains particularly at high temperatures [31]. The ash weight percentages at 600 °C (see Fig. 2d) are 0.3–0.5 wt% lower than the nominal GNP concentration, indicating possible thermal degradation of the nanofillers. This early thermal degradation can be attributed to the existence of defected carbon with lower thermal stability, as revealed via Raman spectroscopy (see

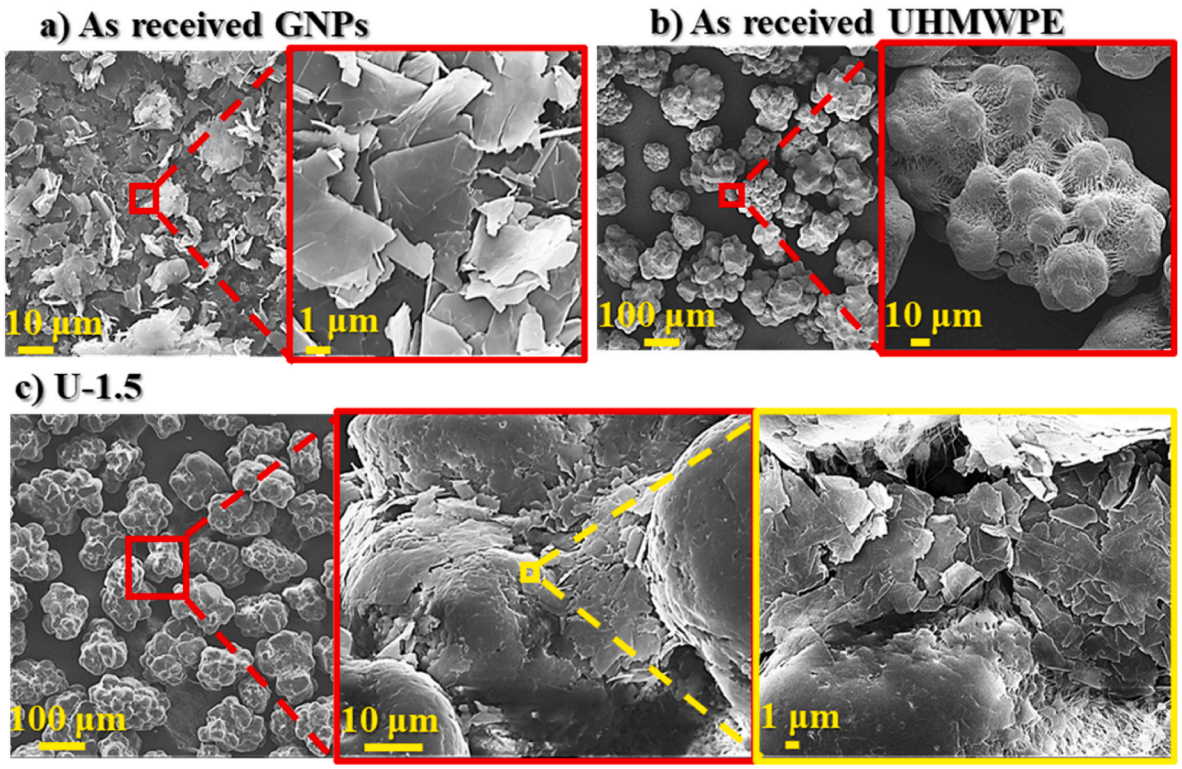

Fig. 1. SEM micrographs of (a) As-received GNPs (b) Neat UHMWPE and (c) Ball-milled GNP/UHMWPE composite powder (U-1.5) at lower and higher magnifications.

Section S2, Supplementary Information).

3.2. Mechanical and piezoresistive responses of GNP/UHMWPE bulk samples

3.2.1. Monotonic tensile loading

Fig. 3a shows the stress-strain responses obtained from the tensile tests performed on the 3D printed GNP/UHMWPE bulk samples. With the addition of GNPs, both the tensile strength (σ_{TS}) and Young's modulus (E) showed significant improvements, reporting σ_{TS} = 16.2 MPa and E = 623 MPa at 1.5 wt% GNP loading (U-1.5, see Fig. 3c), which were, respectively, ~21 % and ~40 % higher than those of the neat UHMWPE. However, the ductility of the composites decreased steadily with increasing GNP loading because the embedded GNPs impede the mobility of the long polymer chains in the UHMWPE matrix. When the GNP loading was increased to 2 wt% (U-2, see Fig. 3c), reductions in mechanical properties were observed, especially in σ_{TS}, attributed to the presence of larger GNP agglomerates and pores, which act as defects and thus attract stress concentrations and simultaneously reduce the size of the effective load-bearing cross-section. This is corroborated by the SEM images presented in Fig. 4 which show agglomerated GNPs protruding out of the (cryogenically) fractured surfaces of the U-2 sample (Fig. 4d), while the SEM images of the U-1 and U-1.5 samples (Fig. 4b and c) revealed a more uniform dispersion of GNPs. Moreover, the fracture surface of the neat U-0 showed a few relatively large pores with diameters of 100–200 μm (see Fig. 4a, left panel).

The observed improvements in the modulus and tensile strength of the samples brought about by the dispersed GNPs (Fig. 3a, c) can be mainly attributed to three aspects: (i) the increase in the crystallinity of the UHMWPE matrix, as described in **Section 3.1** (see Table 2), (ii) the reinforcing effect of the dispersed GNPs, and (iii) improved densification of the samples during the sintering process. To elaborate on the third aspect, we present, in Fig. 5, μCT images of all compositions including color maps of the pore volume detected in the 3D printed samples within a selected volume of interest (~8 × 3.5 × 1 mm^3). In the case of the pristine U-0 sample, notable pores with volumes of up to 0.08 mm^3 and a substantial porosity of approximately 15 % were evident (see Fig. 5a). However, with the introduction of GNPs, there was a significant enhancement in sample densification during SLS, resulting in a reduced porosity of ~0.35 % at a 1.5 wt% GNP loading (as depicted in Fig. 5c). This observed trend is notably positive, in contrast to the typical expectations in the fused filament fabrication of composites. The latter reduction in porosity (by ~97.5 %) can be attributed to the fact that the GNP/UHMWPE powders absorb a higher amount of laser energy and conduct the heat more efficiently as compared to the neat UHMWPE [26]. This facilitates the fusion and flow of powder particles and therefore enhances the densification of the printed parts. Moreover, the GNPs can help in reducing the inter-particle friction due to their lubricity and this can improve the melt flow (until a certain concentration) despite an increase in melt viscosity, as reported in the literature [26, 32]. However, when the GNP loading was further increased, the sintering quality of the 3D printed parts deteriorated, as seen from the μCT image of the U-2 sample (see Fig. 5d) which revealed a porosity of ~4 %. For the latter sample, it is hypothesized that the presence of agglomerated GNPs on the powder particles hindered the flow of the polymer during the sintering process, which could be a possible reason for the lack of densification.

To better understand the role of the porosity on the mechanical properties, we proceed to compare the measured elastic moduli of the laser-sintered GNP/UHMWPE composites to the predictions of the scaling equation developed specifically for sintered materials by Buch and Goldschmidt [33]:

$$\frac{E_p}{E} = 1 - \frac{15(1-\nu)\varphi_p}{(7-5\nu)+2(4-5\nu)\varphi_p} \tag{3}$$

where E_p is the predicted modulus of the porous sintered material, φ_p is the volume fraction of pores (also referred to as porosity), and E and ν

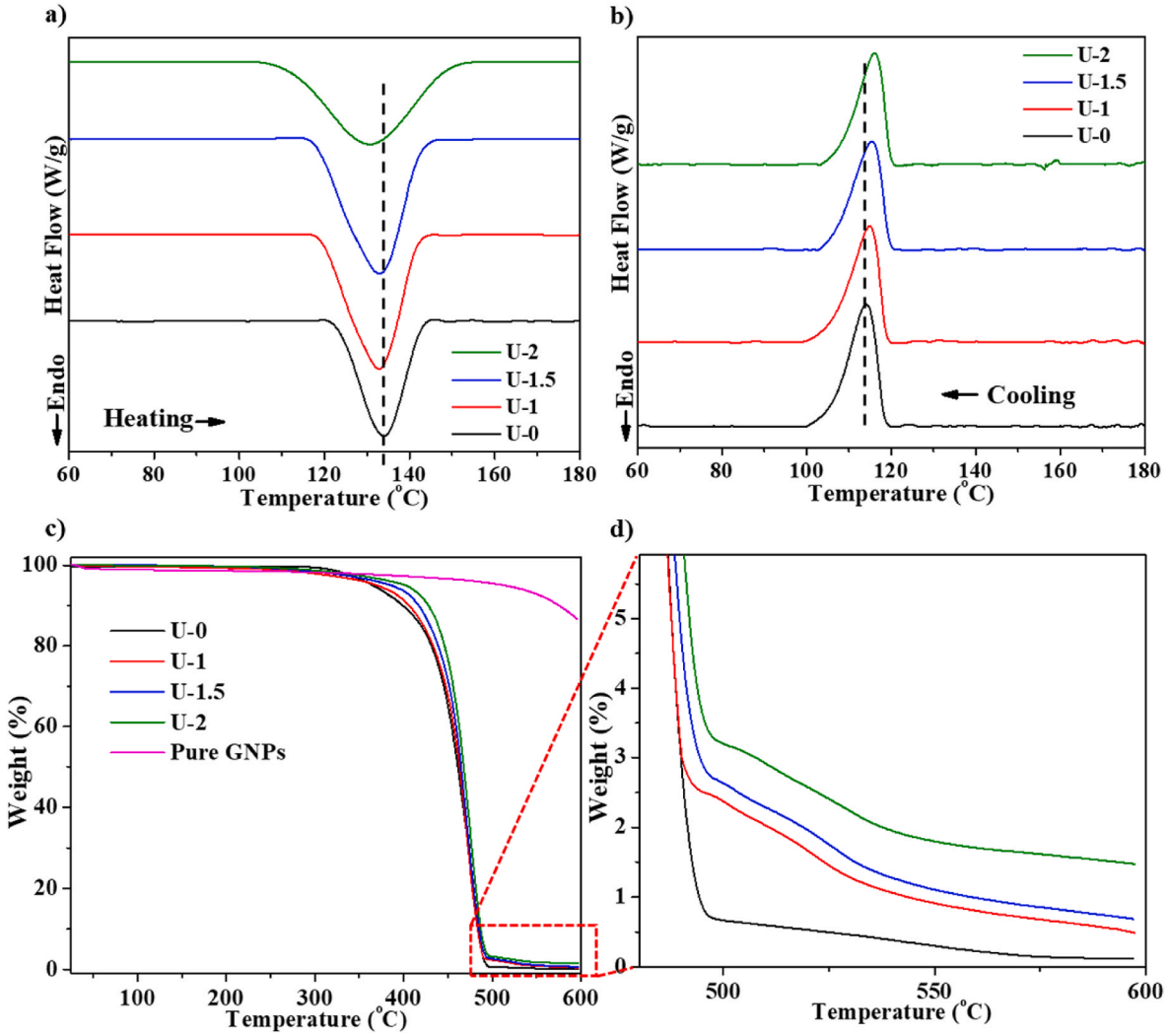

Fig. 2. Thermal characteristics of GNP/UHMWPE composite powders: (a, b) DSC results for the 2nd heating and cooling cycles; (c) TGA results for a temperature range of 25–600 °C with a magnified view (d) showing the residue at higher temperatures.

Table 2
Summary of DSC and TGA data for the neat UHMWPE and GNP/UHMWPE composites: T_m is the melting temperature, T_c is crystallization temperature, ΔH_m is melting enthalpy, X is crystallinity (%) and T_d is thermal degradation temperature. The indices 1 and 2 denote the first and second heating scans, respectively.

Sample ID	Tm_1 (°C)	Tm_2 (°C)	T_c (°C)	ΔHm_2 (J/g)	X (%)	T_d (°C)	*Ash* (%)
U-0	143	134.2	114	110.4	38.2	462	0
U-1	142	133	115	135.8	47	463	0.5
U-1.5	141.5	132.7	115.5	141.6	49	465	0.7
U-2	141	130.7	116	132.9	46	468	1.5

are the Young's modulus and Poisson's ratio of the fully dense bulk material, respectively. In the following, we neglect the intrinsic changes in the modulus of the composite due to the addition of GNPs, and thus assume $E = E_m$ where E_m represents the measured modulus of the fully-dense neat UHMWPE sample. Further, the Poisson's ratio of UHMWPE is assumed to be $\nu = 0.4$ [1]. Since a fully dense UHMWPE could not be produced via SLS in this study, E was estimated by setting E_p and φ_p in **eq. (3)** to the measured modulus (444 MPa) and porosity (0.15) of the sintered neat U-0 sample, respectively. On solving for E, we obtain $E = E_m = 585$ MPa.

Fig. 6 compares the modulus predictions E_p to the values measured for the laser-sintered GNP/UHMWPE composites with 0, 1, 1.5 and 2.0 wt% GNPs; the corresponding numerical values are presented in Table S2 (Supplementary Information). Overall, the predictions of eq. (3) seem to adequately capture the measured changes in the modulus with increasing GNP content. However, the predictions show a plateau in the modulus between 1 and 1.5 wt% GNP loading, but the measured values increased significantly over the same range. As the samples containing 1 and 1.5 wt% GNPs consistently exhibited a porosity level of ~0.4 % (see Table S2), the observed rise in modulus within this range can be solely attributed to two factors: the concurrent increase in the crystallinity of the UHMWPE matrix and the reinforcing influence of the incorporated GNPs. It's worth noting that this behavior can be effectively modeled by employing appropriate values of the elastic modulus (E) and Poisson's ratio (ν) for fully dense bulk composites, which vary in relation to the GNP loading. Since the GNPs are coated on the surface of the UHMWPE powder, it is anticipated that the GNPs form a segregated reinforcing network in the UHMWPE matrix after sintering, once a critical GNP concentration is reached. At higher GNP loading (≥2 wt%), both the predictions and measurements show a similar drop in the modulus due to the increased level of porosity (~4 %). It should be mentioned that larger GNP agglomerates can also act as defects and further degrade the mechanical properties of the composite. However, this effect is considered less significant than the increase in the overall

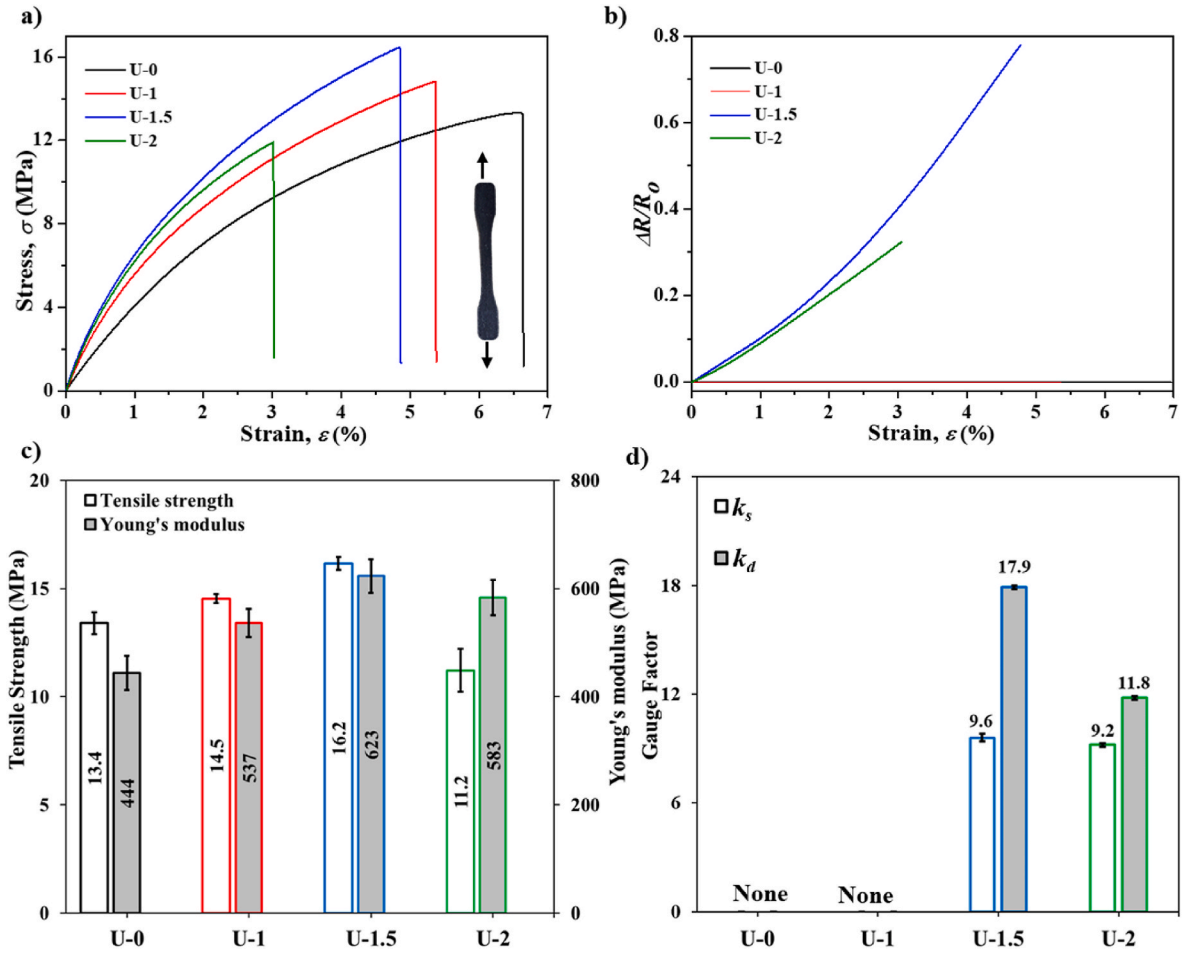

Fig. 3. Mechanical and piezoresistive behaviors of GNP/UHMWPE composites subject to uniaxial tension: (a, b) measured engineering stress vs. engineering strain and $\Delta R/R_0$ vs. engineering strain curves, (c, d) tensile strength, Young's modulus and gauge factors evaluated in the elastic (k_s) and inelastic (k_d) regions of the stress-strain curve for all compositions.

porosity, due to the relatively lower concentration of GNPs added to the composites.

The piezoresistive responses of the GNP/UHMWPE samples measured under uniaxial tensile loading are plotted in Fig. 3b in the form of $\Delta R/R_0$ vs. ε curves, while the corresponding gauge factors (k), as defined in eq. (2), are shown in Fig. 3d for each composition. Note that the k values are calculated in two regions: (i) elastic region ranging from $0 \leq \varepsilon \leq \varepsilon_y$, where ε_y is the yield strain (~1 %), and (ii) inelastic region ranging from $\varepsilon_y \leq \varepsilon \leq \varepsilon_f$, where ε_f is the strain at failure. The k values corresponding to the elastic and inelastic regions are also referred to as strain sensitivity (k_s) and damage sensitivity (k_d), respectively [34]. In Fig. 3b, the piezoresistive responses are only reported for the U-1.5 and U-2 samples, because below 1.5 wt% GNP loading, the electrical conductivity of the samples vanished (see Supplementary Fig. S8). Among the two conductive samples, U-1.5 showed a higher sensitivity in both elastic and inelastic regions due to the more sparsely distributed GNPs, enabling larger resistance changes under tensile loading (in line with the literature [19,35]). Moreover, the U-1.5 sample exhibited a progressively increasing resistance $\Delta R/R_0$ (see Fig. 3b) which can be attributed to the nonlinear characteristics of the tunneling resistance which becomes more dominant at higher strain levels [19,35,36]. Note that similar trends in the mechanical and piezoresistive behaviors were observed under three-point bending, as detailed in **Section S4** (Supplementary Information).

3.2.2. *Cyclic tensile loading*

Cyclic tensile tests with incrementally increasing strain amplitudes were performed to investigate the effect of damage progression on the piezoresistive behavior of the GNP/UHMWPE composites. As seen from Fig. 7a, the measured $\Delta R/R_0$ vs. time history follows a similar pattern as the imposed strain throughout the test. However, the $\Delta R/R_0$ curve shows rather blunt peaks and troughs, unlike the imposed strain history, which can be attributed to configurational changes in the conductive GNP network due to the viscoelastic/viscoplastic behavior of the matrix [19,35]. The evolution of inelastic strain during the test can be more clearly seen from the stress-strain curves in Fig. 7b, which show widening of the hysteresis loops and growing (inelastic) residual strains (ε_r) upon unloading to zero load with increasing strain amplitude. Narrow hysteresis loops are also observed at very small strain amplitudes (≤0.5 %) due to the viscoelastic nature of UHMWPE, which showed a loss factor of 0.1 at room temperature, as confirmed via DMA (see Fig. S5, Supplementary Information). Similar hysteresis loops are observed in the piezoresistive response (see Fig. 7c) which indicates that the GNPs do not instantaneously return to their original relaxed state upon unloading due to viscous damping. It is also seen that the zero-load resistance (upon unloading) increases with the number of cycles which is attributed to the growing residual strains. Interestingly, the $\Delta R/R_0$ values measured at the peak loads and at zero load in each cycle, respectively, match well with the $\Delta R/R_0$ vs. strain curve from the monotonic tensile test (see dotted line in Fig. 7c), indicating that the re-orientation of GNPs is reversible upon unloading, despite the observed hysteretic behavior.

To examine the cyclic stability in the mechanical and functional response, the neat U-0 and the U-1.5 composite were subject to 100

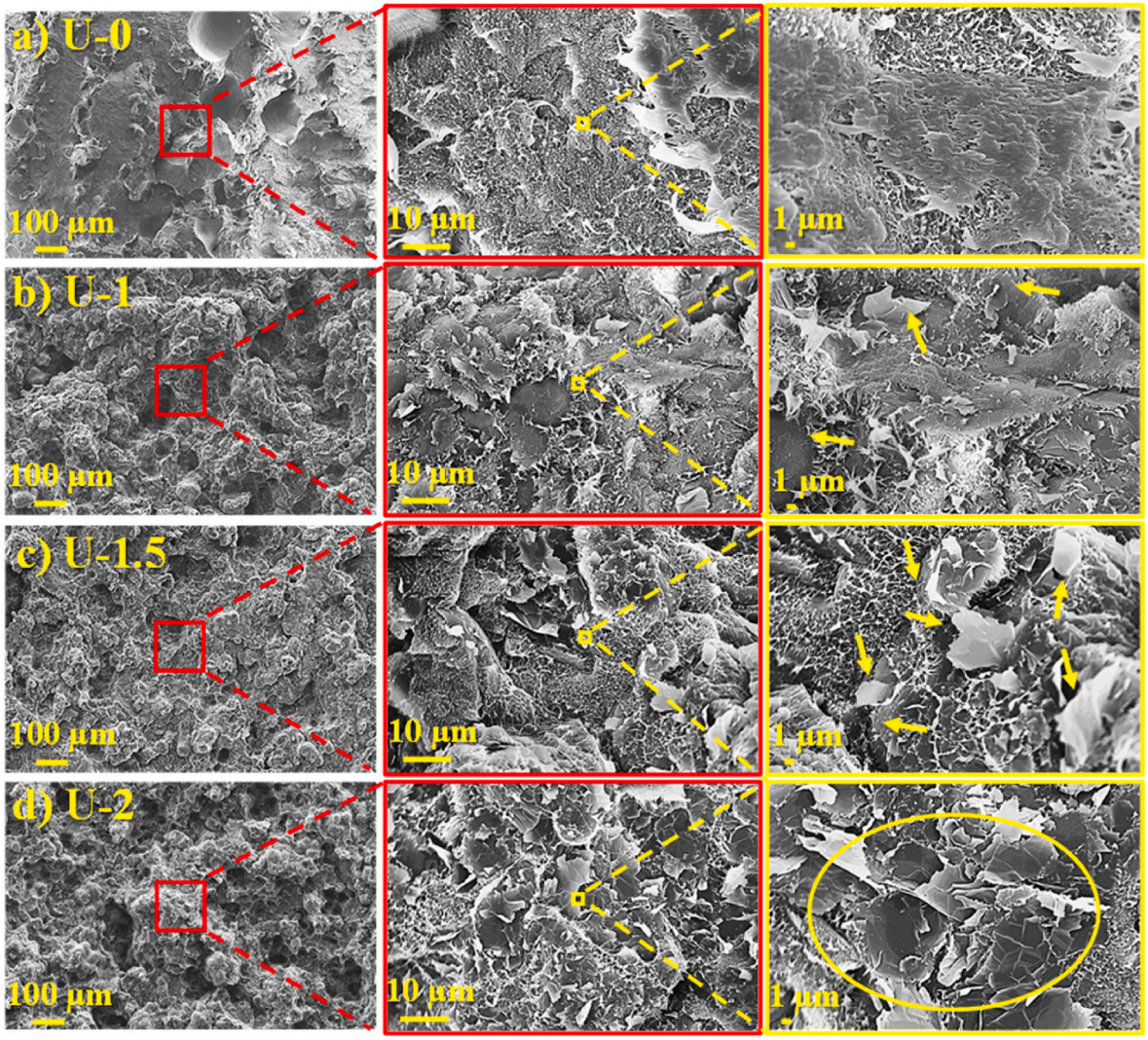

Fig. 4. SEM micrographs of cryogenically fractured neat UHMWPE and GNP/UHMWPE samples at lower and higher magnifications. Note: arrows in (b, c) show GNPs whereas the oval in (d) shows agglomerates of GNPs.

strain-controlled tensile load cycles between the maximum and minimum strain of 2 % and 1 % respectively, and the obtained stress-strain curves are presented in Fig. 7d and e, respectively. For both samples, the maximum stress and the mean stress decay with cycling due to the stress relaxation associated with the constant nonzero mean strain (see black curve in Fig. 7d and e), as reported in previous studies [19,37]. This stress-decaying phenomenon is more pronounced in the first few cycles, after which only modest differences are observed (e.g. stress drops marginally between the 50th and 100th cycle). Both samples, due to their viscoelastic nature, exhibit cyclic softening - a phenomenon where the material shows a reduction in its modulus during the cyclic loading and unloading process, resulting from mechanisms like creep or stress relaxation. Since the hysteresis loops (Fig. 7d and e) become narrower with cycling, the energy dissipated per cycle diminishes and approaches a stationary value after ~60 cycles, as seen from Fig. S9 (Supplementary Information). Overall, the U-1.5 dissipated slightly higher amounts of energy per cycle as compared to the neat U-0, which can be attributed to dissipative processes occurring at the matrix-GNP interfaces which involve slippage and friction, as reported in previous studies [38–40].

The corresponding $\Delta R/R_0$ vs. time history is plotted in Fig. 7f along with the imposed strain history. Like the stress response, the $\Delta R/R_0$ peaks decay with the accumulation of load cycles, particularly during the initial phase of the test. This is attributed to the rearrangement of the conductive network due to the segmental motion of the polymer chains in the surrounding UHMWPE matrix. Following the initially applied strain, the chains gradually return to their more entropically favored configuration as the cycling proceeds, and the sample (partially) gains back its original conductivity [19]. However, the $\Delta R/R_0$ curve in Fig. 7f shows well-matched slopes throughout the test (see inset), which is a desired attribute for strain sensing applications.

3.3. *Mechanical and piezoresistive responses of GNP/UHMWPE 2D lattice structures*

By utilizing the capability of the SLS process to realize complex structures, we also fabricated 2D lattice structures from the as-prepared GNP/UHMWPE powder considering two different unit cell geometries: (i) hexagonal (Hex), and (ii) reentrant (Re). Note that the re-entrant structure is known to be auxetic (i.e. possesses negative Poisson's ratio) [41] which can be beneficial for various practical applications including elbow/knee pads, or stents, for example. Additionally, honeycombs have been extensively explored as core materials for sandwich structures in numerous fields due to their high strength-to-weight ratio, high stiffness-to-weight ratio, excellent energy absorption and thermal protective characteristics [42,43]. For both the Hex and Re structures,

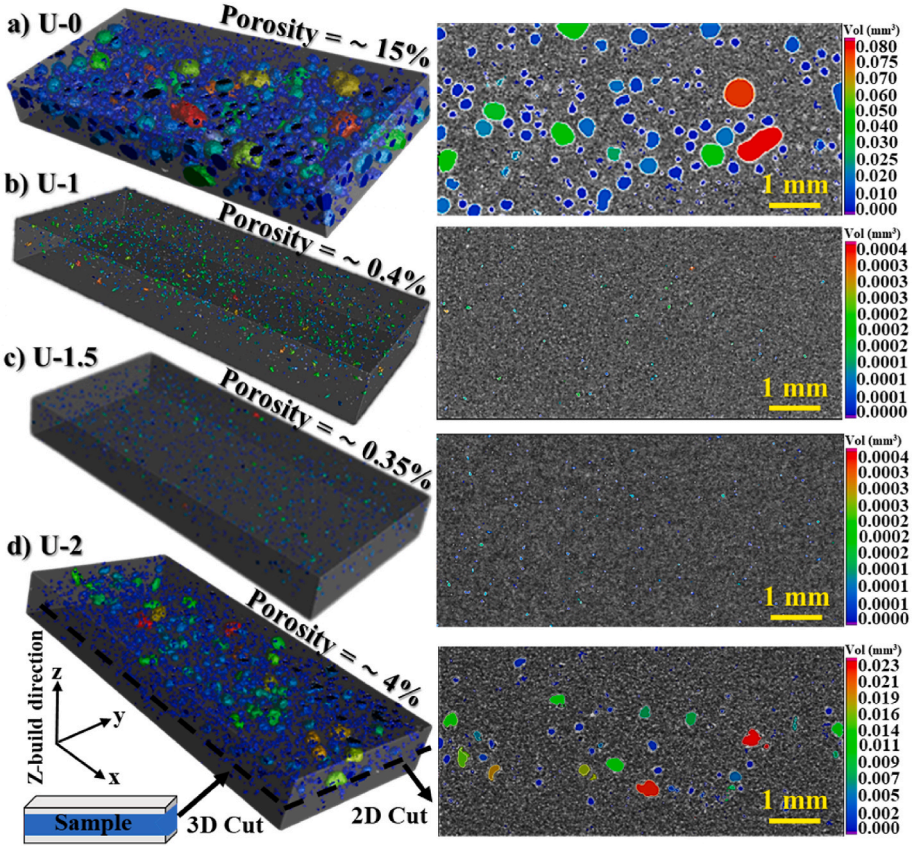

Fig. 5. μCT images of (a) neat UHMWPE and (b–d) GNP/UHMWPE composites showing the pore volume for different GNP loadings.

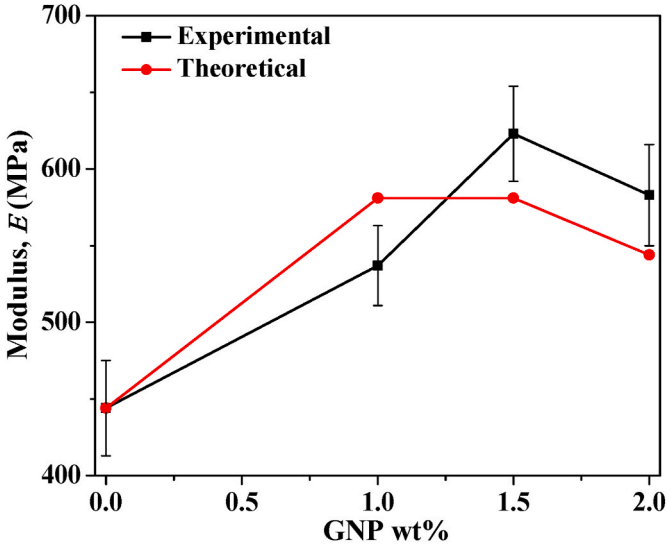

Fig. 6. Theoretical predictions and measurements of the elastic moduli of selectively laser-sintered GNP/UHMWPE with different GNP concentrations.

two different unit cell orientations were considered (see Fig. S10 and Table S1 in Supplementary Information), to evaluate the directional dependence of their mechanical and piezoresistive responses. All the four 2D lattice structures considered in this study were printed with the same relative density (50 %) and composition (1.5 wt% GNP) and are referred to as Hex-1, Hex-2, Re-1 and Re-2, as shown in the inset of Fig. 8a. As seen from Fig. 8a, all the lattice structures failed in a brittle manner near the nodes without showing any significant prior plastic deformation (see Videos **SV1-4**, Supplementary Information). Although the Hex-2 and Re-2 samples failed at smaller strains as compared to their Hex-1 and Re-1 counterparts, the former lattice structures showed higher elastic moduli and tensile strengths (see Table 3) since their struts are more aligned along the loading direction and thus, deform predominantly in the stiffer stretching mode.

Fig. 8b presents the corresponding $\Delta R/R_0$ vs. strain curves, showing nearly linear trends at small strains for the four samples. It is interesting to note that the initial gauge factors (k_s) of the lattice structures (see Table 3) are lower than those of the bulk samples (see Fig. 3d) with the same GNP loading. This can be attributed to the non-uniform strain fields in the lattice struts which experience a combination of bending, shearing and stretching deformations. In the lattice struts subject to larger bending moments, the nanofillers located close to the tensile face tend to separate causing the resistance to increase, while those in the vicinity of the compressive face tend to move closer together, causing the resistance to decrease. Hence, it can be argued that these two opposing effects reduce the overall strain sensitivity of the structure. The latter explanation can also be used to justify the superior strain sensitivities (k_s) of the Hex-2 and Re-2 lattices, as compared to their Hex-1 and Re-1 counterparts, due to the more stretch-dominated behavior of the former structures as a result of their favorable strut alignment. Overall, it is observed that the gauge factors follow similar trends as the measured elastic moduli (see Table 1). It's worth highlighting that the alteration in resistance within the cell walls, influenced by their deformation patterns and the accumulation of damage, plays a pivotal role in determining both the piezoresistive behavior and the sensitivity of the 2D lattice composite structure during tensile loading.

4. Conclusions

In this study, we experimentally investigated the mechanical and

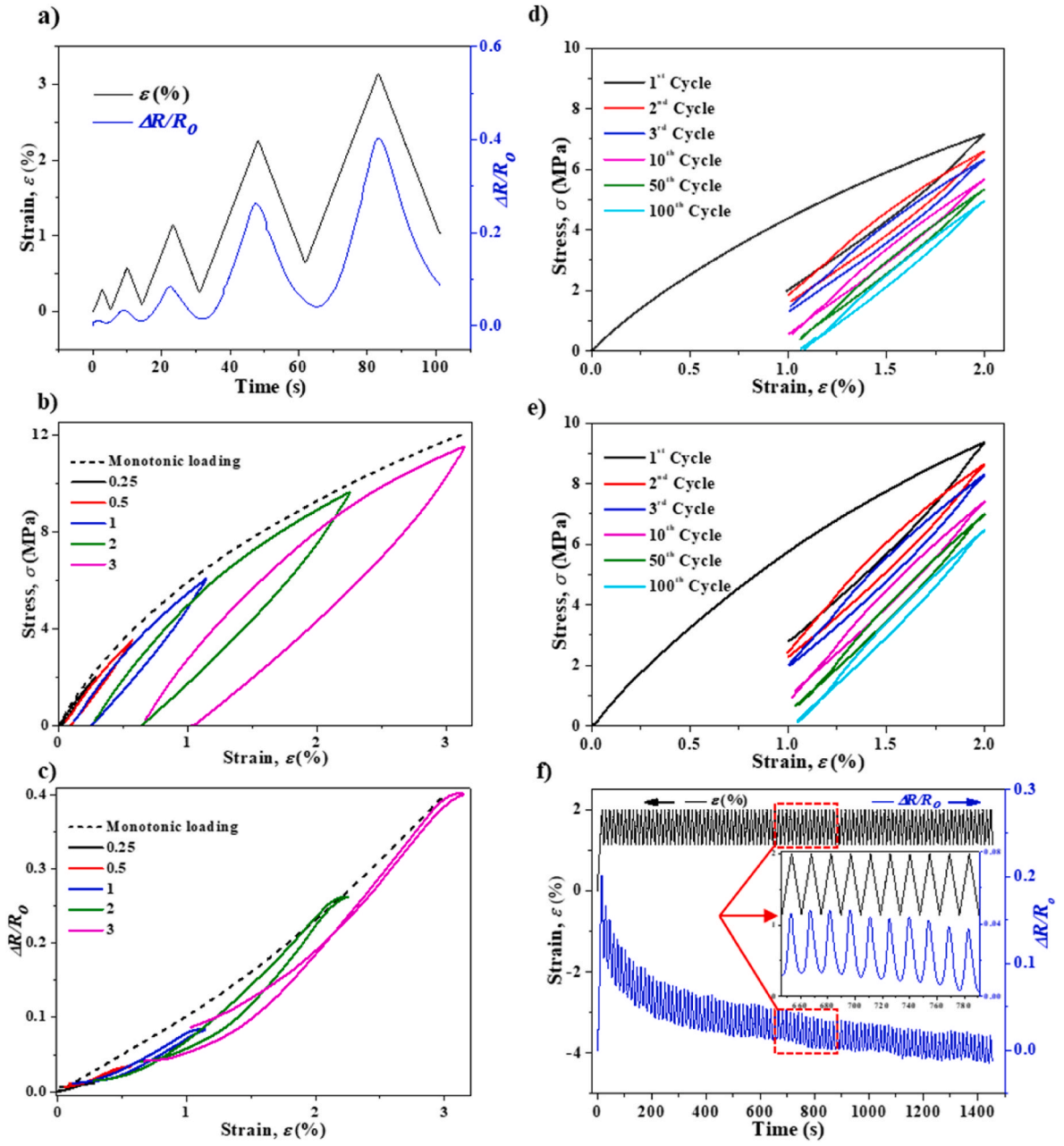

Fig. 7. Mechanical and piezoresistive behaviors of GNP/UHMWPE (U-1.5) subject to (a–c) incremental cyclic tensile loading and (d–f) 100 strain-controlled tensile load cycles.

piezoresistive self-sensing performance of GNP/UHMWPE composites processed via selective laser sintering (SLS). Ball-milled GNP/UHMWPE composite powders prepared with three different GNP loadings (1.0, 1.5 and 1.5 wt%) were used as the feedstock for SLS. The strain- and damage-sensing performances of the 3D-printed bulk structures were evaluated under monotonic and cyclic tensile loading, and the fundamental structure-property-process relations were discussed.

The results revealed that the inclusion of 1.5 wt% GNPs in UHMWPE led to a substantial enhancement of crystallinity (~28 %) and a remarkable reduction in porosity (~98 %) of as-processed specimens. These improvements significantly contributed to increased strength (~21 %) and elastic modulus (~40 %) and were attributed to the improved laser power absorption and thermal conductivity of the embedded GNPs, which facilitated polymer particle fusion and flow during sintering. Additionally, the reinforcing effect of GNPs also contributed to enhanced mechanical performance. However, at higher GNP concentrations (≥2 wt%), porosity increased, and mechanical properties deteriorated due to nanofiller agglomeration. At GNP concentrations of 1.5 wt% and above, the GNP/UHMWPE composites exhibited electrical conductivity and displayed significant piezoresistive behavior. They reported gauge factors as high as 9.6 and 18 in the elastic and inelastic regions, respectively (at 1.5 wt% GNP loading). Under cyclic loading with incrementally increasing strain amplitudes, the GNP/UHMWPE composite exhibited a hysteretic piezoresistive response due to its viscoelastic nature, which led to a delay in the re-orientation of the conductive network during unloading. Additionally, strain-controlled cyclic tests demonstrated that the GNP/UHMWPE composites maintained their piezoresistive functionality over 100 loading cycles.

The GNP/UHMWPE powder with 1.5 wt% GNP loading was also employed to fabricate 2D lattice structures (50 % relative density) with hexagonal and re-entrant topologies. These structures exhibited a nearly

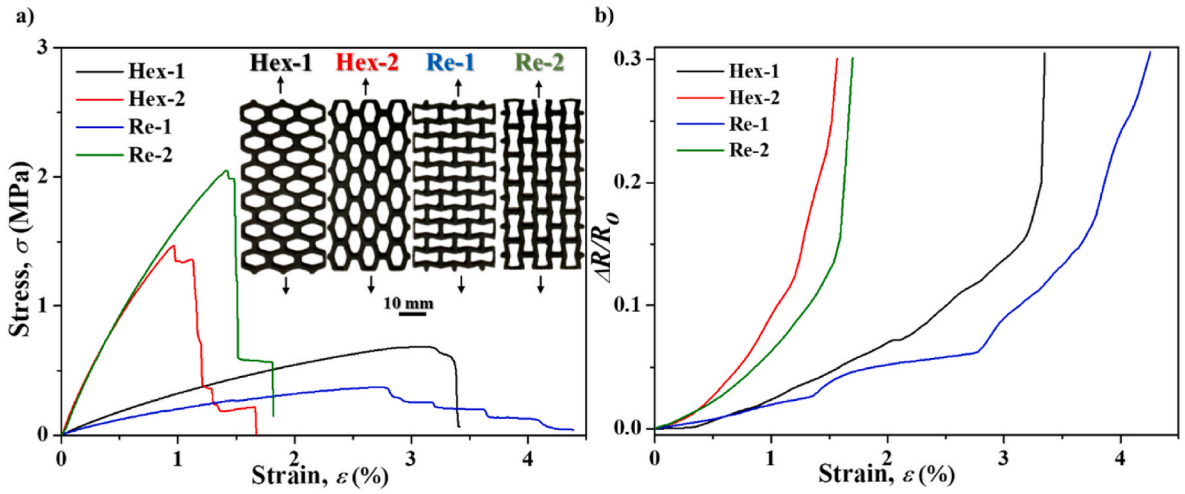

Fig. 8. Mechanical and piezoresistive behaviors of 1.5 wt% GNP/UHMWPE composite 2D lattice structures (50 % relative density) tested under quasi-static uniaxial tension: (a) stress-strain responses, (b) piezoresistive responses.

Table 3
Summary of mechanical and piezoresistive properties of 3D printed hexagonal and re-entrant GNP/UHMWPE (U-1.5) lattice structures subject to uniaxial tension. Note: Average strain sensitivity (k_s) and damage sensitivity (k_d) values were calculated in the regions 0 % $\leq \varepsilon \leq$ 0.5 % and 0.5 % $\leq \varepsilon \leq$ fracture, respectively.

Sample ID	Strength (MPa)	Modulus (MPa)	Failure strain (%)	Gauge factor	
				k_s	k_d
Hex-1	0.8 ± 0.1	38 ± 2	3.9 ± 0.7	0.9 ± 0.3	4.5 ± 1
Hex-2	1.5 ± 0.1	188 ± 4	1.2 ± 0.04	5.4 ± 0.3	13.3 ± 1.1
Re-1	0.4 ± .005	23 ± 2	3.1 ± 0.24	1.5 ± 0.1	2.9 ± 0.5
Re-2	1.8 ± 0.2	182 ± 5	1.6 ± 0.18	3.9 ± 0.5	9.3 ± 1.8

linear piezoresistive response until reaching the point of failure. The gauge factors of the lattice structures were lower than those of the parent composites and followed similar trends as the measured elastic moduli. Our study suggests that SLS is a viable method for producing GNP/UHMWPE composite structures with integrated strain-sensing capabilities. However, further refinement of material composition and processing parameters could enhance the fabrication of more intricate 3D structures, bringing these innovative materials closer to practical applications in self-sensing orthopedic implants.

Data availability

The data will be made available on request.

Declaration of competing interest

The authors declare that they have no known competing financial interests or personal relationships that could have appeared to influence the work reported in this paper.

Acknowledgements

The authors would like to express their appreciation to Khalifa University for the financial support they received in the form of the Competitive Internal Research Award (CIRA) [grant number CIRA-2018-128]. This work was supported in part by the EPSRC Centre, funded by the UK Engineering and Physical Sciences Research Council [grant number EP/R513222/1]. The authors would like to thank Mr. Pradeep George for his technical support with the μCT scans conducted at the Advanced Research and Innovation Center (ARIC) which is funded by STRATA Manufacturing PJSC (a Mubadala company) and Khalifa University.

Appendix A. Supplementary data

Supplementary data to this article can be found online at https://doi.org/10.1016/j.jmrt.2023.12.089.

References

[1] Kurtz S. UHMWPE biomaterials handbook: ultra high molecular weight polyethylene in total joint replacement and medical devices. Cambridge: Academic Press; 2009.
[2] Azam MU, Samad MA. UHMWPE hybrid nanocomposite coating reinforced with nanoclay and carbon nanotubes for tribological applications under water with/without abrasives. Tribol Int 2018;124:145–55. https://doi.org/10.1016/j.triboint.2018.04.003. April.
[3] Changhui S, Aibing H, Yongqiang Y, Di W, Jia-kuo Y. Customized UHMWPE tibial insert directly fabricated by selective laser sintering. Int J Adv Manuf Technol 2016;85(5–8):1217–26. https://doi.org/10.1007/s00170-015-8046-6.
[4] Li Y, He H, Ma Y, Geng Y, Tan J. Rheological and mechanical properties of ultrahigh molecular weight polyethylene/high density polyethylene/polyethylene glycol blends. Adv. Ind. Eng. Polym. Res. 2019;2(1):51–60. https://doi.org/10.1016/j.aiepr.2018.08.004.
[5] Song C, Huang A, Yang Y, Xiao Z, Yu JK. Effect of energy input on the UHMWPE fabricating process by selective laser sintering. Rapid Prototyp J 2017;23(6):1069–78. https://doi.org/10.1108/RPJ-09-2015-0119.
[6] Reddy SK, Kumar S, Varadarajan KM, Marpu PR, Gupta TK, Choosri M. Strain and damage-sensing performance of biocompatible smart CNT/UHMWPE nanocomposites. Mater Sci Eng C 2018;92:957–68. https://doi.org/10.1016/j.msec.2018.07.029. November 2017.
[7] Bekas DG, Hou Y, Liu Y, Panesar A. 3D printing to enable multifunctionality in polymer-based composites: a review. Compos. Part B Eng. 2019;179:107540. https://doi.org/10.1016/j.compositesb.2019.107540. October.
[8] Schneider J, Kumar S. Multiscale characterization and constitutive parameters identification of polyamide (PA12) processed via selective laser sintering. Polym Test 2020;86:106357. https://doi.org/10.1016/j.polymertesting.2020.106357. January.
[9] Goodridge RD, et al. Processing of a Polyamide-12/carbon nanofibre composite by laser sintering. Polym Test 2011;30(1):94–100. https://doi.org/10.1016/j.polymertesting.2010.10.011.
[10] Rimell JT, Marquis PM. Selective laser sintering of ultra high molecular weight polyethylene for clinical applications. J Biomed Mater Res 2000;53(4):414–20. https://doi.org/10.1002/1097-4636(2000)53:4<414::AID-JBM16>3.0.CO;2-M.
[11] Goodridge RD, Hague RJM, Tuck CJ. An empirical study into laser sintering of ultra-high molecular weight polyethylene (UHMWPE). J Mater Process Technol 2010;210(1):72–80. https://doi.org/10.1016/j.jmatprotec.2009.08.016.
[12] Khalil Y, Kowalski A, Hopkinson N. Influence of energy density on flexural properties of laser-sintered UHMWPE. Addit Manuf 2016;10:67–75. https://doi.org/10.1016/j.addma.2016.03.002. March.

[13] Khalil Y, Kowalski A, Hopkinson N. Influence of laser power on tensile properties and material characteristics of laser-sintered UHMWPE. Manuf Rev 2016;3. https://doi.org/10.1051/mfreview/2016015. September.
[14] Azam MU, Schiffer A, Kumar S. Mechanical and piezoresistive behavior of selectively laser sintered MWCNT/UHMWPE nanocomposites. Compos. Part A Appl Sci Manuf 2023;173:107701. https://doi.org/10.1016/j.compositesa.2023.107701. June.
[15] Zhu X, Yang Q. Sintering the feasibility improvement and mechanical property of UHMWPE via selective laser sintering. Plast, Rubber Compos 2020;49(3):116–26. https://doi.org/10.1080/14658011.2020.1718321.
[16] Naebe M, Abolhasani MM, Khayyam H, Amini A, Fox B. Crack damage in polymers and composites: a review. Polym Rev 2016;56(1):31–69. https://doi.org/10.1080/15583724.2015.1078352.
[17] Azam MU, Schiffer A, Kumar S. Piezoresistive behavior of MWCNT/PA12 honeycomb composites processed via selective laser sintering. J Mater Res Technol 2023;26:2319–32. https://doi.org/10.1016/j.jmrt.2023.08.051.
[18] Mora A, Verma P, Kumar S. Electrical conductivity of CNT/polymer composites: 3D printing, measurements and modeling. Compos. Part B Eng. 2020;183:107600. https://doi.org/10.1016/j.compositesb.2019.107600.
[19] Verma P, Ubaid J, Varadarajan KM, Wardle BL, Kumar S. Synthesis and characterization of carbon nanotube-doped thermoplastic nanocomposites for the additive manufacturing of self-sensing piezoresistive materials. ACS Appl Mater Interfaces 2022;14(6):8361–72. https://doi.org/10.1021/acsami.1c20491.
[20] Lahiri D, et al. Graphene nanoplatelet-induced strengthening of ultrahigh molecular weight polyethylene and biocompatibility in vitro. ACS Appl Mater Interfaces 2012;4(4):2234–41. https://doi.org/10.1021/am300244s.
[21] Soldano C, Mahmood A, Dujardin E. Production, properties and potential of graphene. Carbon N. Y. 2010;48(8):2127–50. https://doi.org/10.1016/j.carbon.2010.01.058.
[22] Zhang YW, Ma HL, Zhang QL, Peng J, Li JQ, Zhai ML, Yu Z. Facile synthesis of well-dispersed graphene by γ-ray induced reduction of graphene oxide. J. Mater. Chem 2012;22(26):13064–9.
[23] Zhang Y, et al. Cytotoxicity effects of graphene and single-wall carbon nanotubes in neural phaeochromocytoma-derived PC12 cells. Am. Chemcial Soc. 2010;4(6):3181–6.
[24] Ronca A, et al. Selective laser sintering fabricated thermoplastic polyurethane/graphene cellular structures with tailorable properties and high strain sensitivity. Appl Sci 2019;9(5):1–15. https://doi.org/10.3390/app9050864.
[25] Yazdani B, Chen B, Benedetti L, Davies R, Ghita O, Zhu Y. A new method to prepare composite powders customized for high temperature laser sintering. Compos Sci Technol 2018;167:243–50. https://doi.org/10.1016/j.compscitech.2018.08.006. June.
[26] Binling Chen OG, Davies Richard, Liu Yaan, Yi Nan, Qiang Dayuan, Zhu Yanqiu. Laser sintering of graphene nanoplatelets encapsulated polyamide powders. Addit Manuf 2020;35:1013.
[27] Goodridge RD, Tuck CJ, Hague RJM. Laser sintering of polyamides and other polymers. Prog Mater Sci 2012;57(2):229–67. https://doi.org/10.1016/j.pmatsci.2011.04.001.
[28] Yuan S, Bai J, Chua CK, Wei J, Zhou K. Material evaluation and process optimization of CNT-coated polymer powders for selective laser sintering. Polymers 2016;8(10):1–17. https://doi.org/10.3390/polym8100370.
[29] Bai J, Goodridge RD, Hague RJM, Song M. Improving the mechanical properties of laser-sintered polyamide 12 through incorporation of carbon nanotubes. Polym Eng Sci 2013;53:1937–46. https://doi.org/10.1002/pen.
[30] Kurtz SM. UHMWPE biomaterials handbook. second ed. Boston: Academic Press; 2009.
[31] Dorigato A, Brugnara M, Pegoretti A. Novel polyamide 12 based nanocomposites for industrial applications. J Polym Res 2017;24(6):1–13. https://doi.org/10.1007/s10965-017-1257-9.
[32] Sivadas BO, Ashcroft I, Khlobystov AN, Goodridge RD. Laser sintering of polymer nanocomposites. Adv. Ind. Eng. Polym. Res. 2021;4(4):277–300. https://doi.org/10.1016/j.aiepr.2021.07.003.
[33] Buch A, Goldschmidt S. Influence of porosity on elastic moduli of sintered materials. Mater. Sci. Eng. 1970;5(2):111–8. https://doi.org/10.1016/0025-5416(70)90040-6.
[34] Ubaid J, Schneider J, Deshpande VS, Wardle BL, Kumar S. Multifunctionality of nanoengineered self-sensing lattices enabled by additive manufacturing. Adv Eng Mater 2022;24(7). https://doi.org/10.1002/adem.202200194.
[35] Kumar S, Gupta TK, Varadarajan KM. Strong , stretchable and ultrasensitive MWCNT/TPU nanocomposites for piezoresistive strain sensing. Compos. Part B 2019;177:107285. https://doi.org/10.1016/j.compositesb.2019.107285. August.
[36] Reddy SK, Kumar S, Varadarajan KM, Marpu PR, Gupta TK, Choosri M. Strain and damage-sensing performance of biocompatible smart CNT/UHMWPE nanocomposites. Mater Sci Eng C 2018;92:957–68. https://doi.org/10.1016/j.msec.2018.07.029. July.
[37] Arzhakov M. Relaxation in physical and mechanical behavior of polymers. CRC Press; 2019.
[38] Gardea F, Glaz B, Riddick J, Lagoudas DC, Naraghi M. Energy dissipation due to interfacial slip in nanocomposites reinforced with aligned carbon nanotubes. ACS Appl Mater Interfaces 2015;7(18):9725–35. https://doi.org/10.1021/acsami.5b01459.
[39] Katsiropoulos CV, Pappas P, Koutroumanis N, Kokkinos A, Galiotis C. Enhancement of damping response in polymers and composites by the addition of graphene nanoplatelets. Compos Sci Technol 2022;227:109562. https://doi.org/10.1016/j.compscitech.2022.109562. May 2021.
[40] Gardea F, Glaz B, Riddick J, Lagoudas DC, Naraghi M. Thermally activated energy dissipation in semi-crystalline polymer nanocomposites. Compos Sci Technol 2016;134:275–86. https://doi.org/10.1016/j.compscitech.2016.08.025.
[41] Kumar N, Panda B, Kumar S. In-plane energy absorption characteristics of a modified re-entrant auxetic structure fabricated via 3D printing. Compos. Part B 2022;228:109437. https://doi.org/10.1016/j.compositesb.2021.109437. September 2021.
[42] Kumar S, Ubaid J, Abishera R, Schiffer A, Deshpande VS. Tunable energy absorption characteristics of architected honeycombs enabled via additive manufacturing. ACS Appl Mater Interfaces 2019;11(45):42549–60. https://doi.org/10.1021/acsami.9b12880.
[43] Andrew JJ, Schneider J, Ubaid J, Velmurugan R, Gupta NK, Kumar S. Energy absorption characteristics of additively manufactured plate-lattices under low-velocity impact loading. Int J Impact Eng 2021;149:103768. https://doi.org/10.1016/j.ijimpeng.2020.103768. April 2020.